Computation of transverse-electric polarized optical eigenstates in dielectric systems based on perfectly matched layer

Tianpeng Jiang [1,*] and Yang Xiang[1,2,†]

[1]*Department of Mathematics, The Hong Kong University of Science and Technology, Clear Water Bay, Kowloon, Hong Kong SAR, China*
[2]*HKUST Shenzhen-Hong Kong Collaborative Innovation Research Institute, Futian, Shenzhen, China*

The optical resonance problem is an eigenproblem with an exponential-growing boundary condition imposed at infinity. This inconvenient boundary condition is caused by the openness of dielectric systems, and it is explained as the effect of retardation. Following our previous work [Jiang and Xiang, Phys. Rev. A **102**, 053704 (2020)] where a perfectly-matched-layer method is developed for transverse-magnetic modes, we extend the method in this paper to transverse-electric modes and apply it to study mode symmetries. The method is implemented by introducing an extra layer to absorb outgoing waves at the far-field region, based on which we derive a damping eigenequation. A finite-element-based numerical approach is developed to compute the eigenstates of the damping eigenproblem. Our method is validated by application to the circular cavity and comparison with exact analytical solutions of whispering-gallery modes. We apply the method to the elliptic cavity to study the even- and odd-symmetric optical eigenstates. We also apply the method to trace the evolution of a pair of degenerate eigenstates with cavity shapes smoothly deformed from circles to squares.

I. INTRODUCTION

With the rapidly progressing fabrication technology in silicon-on-insulator platforms [1], dielectric microcavities [2] are developed as building blocks in a wide variety of on-chip optical devices, such as optical filters [3], photonic circuits [4,5], microlasers [6,7], biomedical sensors [8,9], optical gyroscopes [10], etc. Most applications are making use of a cavity's resonance phenomena due to the fact that resonance states are sensitive to dielectric perturbations, for example cavity deformations [11,12], nanoparticle perturbations [9], and index variations [13,14]. The resonance states formed in dielectric cavities are energy-dissipating processes, which cause the effective Hamiltonian of the optical resonance system to be non-Hermitian [15–17]. Uncommon physical phenomena, such as wave chaos [18,19] and exceptional points [20,21], could happen in this non-Hermitian system.

Exact analytical solutions of optical eigenstates in dielectric cavities do not exist in general, except for those with regular shapes: for example, circular shapes [22,23] and square and rectangular shapes [24,25]. For dielectric cavities deformed from regular shapes, perturbation theories can be applied to obtain analytical approximations for their eigenstates. A perturbation approach was developed based on an artificially constructed ansatz for cavities with mirror-symmetric shapes [11], and then this ansatz was generalized to asymmetric cavities [26]. Another perturbation approach employed rigorous perturbation series without presumed ansatz formulation [12], and this method was successfully applied to calculate eigenstates in limaçon and spiral cavities. However, for largely deformed cavities, the perturbation approach gradually loses its accuracy because the error increases. A possible solution to this issue is to use high-order perturbation corrections, but such perturbation expressions could be extremely complex. An alternative approach is to seek numerical solutions.

For arbitrarily shaped cavities, numerical methods provide an efficient treatment to calculate the optical eigenstates. Numerical approaches based on boundary-element methods (BEMs) have been developed [27]. It has been discussed that spurious solutions exist in the BEMs [27]. Recently, the authors developed a finite-element-based method to compute optical eigenstates [28], and this method has been successfully applied to study the evolution of eigenstates near exceptional points. The developed approach is only applicable to transverse-magnetic modes. In this paper, we extend the method to transverse-electric modes, and we apply it to study the symmetries of optical eigenstates in deformed cavities.

Note that although both the resonance problems and the time-steady Schrödinger equation in quantum-mechanical systems are eigenproblems, they are essentially different. Dielectric systems are intrinsically lossy because optical cavities are open systems with energy continuously radiating to infinity. This openness causes eigenfunctions to grow exponentially at infinity due to the effect of retardation [28,29]. In contrast, quantum-mechanical systems are closed systems with total energy conserved, therefore their wave functions are restricted in a certain Hilbert space, hence they are square-integrable. This difference makes it difficult to formulate optical resonance problems under the framework of quantum mechanics [30]. To calculate optical eigenstates, a special

*tjiangad@connect.ust.hk
†maxiang@ust.hk

framework is needed to resolve the issue of exponential-growing eigenfunctions.

The perfectly-matched-layer (PML) method is an ideal technique to transform eigenfunctions from exponential growing to exponential decaying. The PML is an artificially constructed layer at the far-field region to absorb outgoing waves, which is often set up for computational convenience in solving acoustic and electromagnetic wave equations. The PML method is first introduced by Bérenger for the scattering problems [31,32], and the original formulation involves splitting the field equations in the PML. Subsequent formulations avoid this splitting and interpret it as the complex-coordinate stretching [33]. Based on the complex-stretching technique, PML methods for curvilinear coordinates have been developed [34–36] and optimized [37]. Analysis of the existence and uniqueness of PML solutions was performed [38,39]. The PML methods have also been adopted to solve resonance problems in fluid dynamics [40], aeroacoustics [41], and electromagnetics [42–45].

In the computation of optical problems, the PML methods have been applied to complex optical structures, e.g., one-dimensional waveguides [46], gratings [47], plasma resonators [48], periodic structures [49], etc. In our previous work [28], we have successfully applied the PML method to study optical eigenstates of transverse-magnetic (TM) modes in two-dimensional (2D) dielectric systems. In this paper, we are going to apply the PML method to compute optical eigenstates of transverse-electric (TE) modes in 2D dielectric systems.

The main mechanism of this method is to introduce an absorption layer at the far-field region. When waves penetrate into this layer, they are absorbed as they propagate forward. This complex-coordinate stretching technique transforms the eigenfunctions from exponential growing into exponential decaying, as well as transforming the original eigenequation into the damping eigenequation. We then derive a weak form of the damping equation on a truncated region. Based on the weak form, we develop a finite-element method to solve the damping eigenproblem. The solutions to the damping eigenproblem are also solutions to the original problem.

We validate the developed PML method by applying it to compute the optical eigenstates in the circular cavity. Exact analytical solutions exist for eigenstates in the circular cavity, and they are called whispering-gallery modes (WGMs) [22,23]. The eigensolutions computed by the PML method agree perfectly with those of WGMs, which validates the PML method developed in this paper. We then apply the PML method to the elliptic cavity to study the chaotic optical eigenstates. The axial symmetries, i.e., *even-* and *odd*-symmetry, of eigenstates in elliptic cavities are studied. Finally, we apply the PML method to trace a pair of degenerate eigenstates when the cavity gradually deforms from a circular shape to a square shape. We find that the pair of degenerate eigenstates evolve in completely different directions, while they preserve the *even* and *odd* axial symmetries throughout the cavity-shape deformation.

The PML method developed in this paper is applicable to arbitrary dielectric distributions, which enables robust calculations of optical eigenstates in largely deformed cavities, multicavities, random media, index-varying dielectric systems, etc. The PML method transforms the eigenfunctions of optical resonance problems from exponential growing into exponential decaying, hence square-integrable. This builds up a framework to formulate the non-Hermitian optical resonance problems, which can be further solved using traditional methods.

The rest of this paper is organized as follows. In Sec. II, we review the resonance problems in terms of their eigenequation and boundary conditions, and we explain the exponential-growing boundary condition as the effect of retardation. In Sec. III, we develop the PML approach by introducing the damping function, performing the complex-coordinate stretching, and deriving the damping eigenequation. In Sec. IV, we derive the weak form to implement the finite-element method to compute the eigenstates. In Sec. V, we apply the PML method to compute eigenstates in three examples. Section VI presents conclusions.

II. RESONANCE PROBLEMS

On-chip optical devices are fabricated on thin layers of materials with thickness far less than in-plane dimensions. Therefore, formulating the original three-dimensional (3D) resonance problem in the in-plane (r, θ) coordinates would be convenient for modeling. By using the variable-separation method [50], the original 3D problem can be split into two equations: a 1D Helmholtz equation for vertical modes in the z-axis, and a 2D Helmholtz equation for horizontal modes in (r, θ) coordinates. Since optical modes form in a vertical dimension, the refractive index in the 2D Helmholtz equation should be replaced by the effective refractive index. Based on this fact, the material's permittivity is approximated by a function independent of the vertical dimension (z-axis) for the 2D problem, and we denote the material's relative permittivity as $\varepsilon(r, \theta)$. We also consider the material's relative magnetic permeability being constant 1 in the whole 2D space, because the material's magnetic responses are negligible in the optical wavelength regime. Both the permittivity and the permeability are considered isotropic in this paper.

Optical eigenstates are the time-steady solutions of Maxwell's equations. By considering monochromatic factors $e^{-i\omega t}$ in both electric fields $\boldsymbol{E}$ and magnetic fields $\boldsymbol{B}$, Maxwell's equations reduce to resonance equations. Here $\omega = kc$ is the resonance frequency, k is the wave number, and c is the light speed in vacuum. By using the effective-index approach, the resonance equation is decoupled into two types of polarized modes [50,51]: the TM modes and the TE modes.

For the TM modes, the in-plane components of magnetic fields and the z-component of electric fields exist while all other components vanish:

$$E_r = 0, \quad E_\theta = 0, \quad E_z = \psi(r, \theta), \tag{1a}$$

$$B_r = -\frac{i}{\omega r}\frac{\partial \psi}{\partial \theta}, \quad B_\theta = \frac{i}{\omega}\frac{\partial \psi}{\partial r}, \quad B_z = 0, \tag{1b}$$

in which the z-component of electric fields satisfies the eigenequation

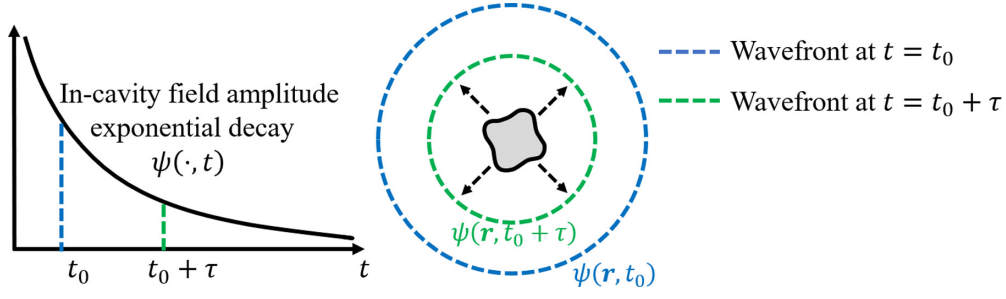$$\nabla^2 \psi(r, \theta) + k^2 \varepsilon(r, \theta)\psi(r, \theta) = 0. \tag{2}$$

FIG. 1. Illustration of the retardation effect. The left panel is the field amplitude inside the cavity in the time domain, and the right panel shows the wavefront sequence in the spatial domain.

For the TE modes, the in-plane components of electric fields and the z-component of magnetic fields exist while all other components vanish:

$$B_r = 0, \quad B_\theta = 0, \quad B_z = \psi(r, \theta), \tag{3a}$$

$$E_r = \frac{ic^2}{\omega} \frac{1}{r\varepsilon(r, \theta)} \frac{\partial \psi}{\partial \theta}, \quad E_\theta = -\frac{ic^2}{\omega} \frac{1}{\varepsilon(r, \theta)} \frac{\partial \psi}{\partial r}, \quad E_z = 0, \tag{3b}$$

in which the z-component of magnetic fields satisfies the eigenequation

$$\nabla \cdot \left(\frac{1}{\varepsilon(r, \theta)} \nabla \psi(r, \theta) \right) + k^2 \psi(r, \theta) = 0. \tag{4}$$

In the eigenequations (2) and (4), k^2 is the eigenvalue and $\psi(r, \theta)$ is the eigenfunction.

The optical eigenstates formed in the dielectric cavities are leaky states. Once the eigenstates are excited, there is no energy supply. In the meantime, because of the openness of dielectric systems, energy carried by electromagnetic waves keeps radiating to infinity. Therefore, the total electromagnetic energy inside the cavity is exponentially decaying in time. In viewing the monochromatic factor $e^{-i\omega t} = e^{-i \operatorname{Re}(k)ct} e^{\operatorname{Im}(k)ct}$, the leaky property of eigenstates implies that the wave number k is a complex value with the imaginary part being negative, i.e., $\operatorname{Im}(k) < 0$. We denote $k = k_r - ik_i$ for some $k_r, k_i > 0$ to be determined by the eigenproblem. The real part k_r is the resonance frequency, and the imaginary part k_i is the decay rate of the eigenstate. Once the eigenvalue is determined, the quality factor Q of the eigenstate can be derived as

$$Q = k_r/(2k_i). \tag{5}$$

The temporally exponential decaying would cause spatially exponential growing. This is explained as the effect of retardation [28,29], as illustrated in Fig. 1. The energy of the eigenstate is initially contained inside the dielectric cavity. With time evolves, energy radiates to infinity in the form of one-by-one wavefronts, thus the energy within the cavity is decaying. Because the energy of each wavefront is proportional to the instantaneous total energy contained in the cavity, the wavefront formed earlier (hence propagating further away) carries more energy. Therefore, in view of the spatial domain at a fixed time, the field components are exponentially growing at the far-field region.

While the intuitive explanation is given as the effect of retardation, the quantitative description is expressed by the radiation boundary condition (BC) [28]: as $r \to +\infty$,

$$\psi(r, \theta) \sim \frac{F(\theta)}{\sqrt{r}} e^{in_0 kr} = \frac{F(\theta)}{\sqrt{r}} e^{in_0 k_r r} e^{n_0 k_i r}, \tag{6}$$

where $n_0 > 0$ is the refractive index of materials at infinity. Here the dielectric permittivity is assumed to be constant at infinity:

$$\lim_{r \to +\infty} \varepsilon(r, \theta) = n_0^2. \tag{7}$$

In the BC Eq. (6), $F(\theta)$ is the far-field pattern denoting the directional distribution of the eigenstate, $e^{in_0 k_r r}$ is the spatial oscillating term, and $e^{n_0 k_i r}$ is the exponential growing term denoting the retardation effect. The denominator $\sqrt{r}$ is to reflect the fact that the energy of each wavefront in the far-field region spreads along the cylindrical perimeter $2\pi r$, indicating that the radial component of the Poynting vector $\boldsymbol{S}$ is proportional to $1/r$:

$$\boldsymbol{S} \cdot \boldsymbol{e}_r = -(E_z e^{-i\omega t})^* B_\theta e^{-i\omega t} \sim \frac{n_0}{c} \frac{|F(\theta)|^2}{r} \quad \text{for TM,} \tag{8a}$$

$$\boldsymbol{S} \cdot \boldsymbol{e}_r = (E_\theta e^{-i\omega t})^* B_z e^{-i\omega t} \sim \frac{c}{n_0} \frac{|F(\theta)|^2}{r} \quad \text{for TE.} \tag{8b}$$

We remark here that in Eq. (8), $F(\theta)$ stands for the far-field pattern of the electric fields and the magnetic fields for TM modes and TE modes, respectively. Therefore, the expressions of the Poynting vector in terms of $F(\theta)$ are slightly different for TM and TE modes.

There are two reasons that the resonance problems are difficult to solve by directly applying numerical methods. First, the problem is defined on the entire domain $\mathbb{R}^2$, and it is improper to truncate the infinite domain into a finite region due to the exponential growth BC. Second, the exponential-growing BC is difficult to implement directly in numerical methods. The PML method is ideal to simultaneously overcome the two difficulties: it transforms the exponential-growing BC into exponential-decaying BC, which enables the truncation of the infinite domain into a finite region. In this paper, we focus on using the PML methods computing optical eigenstates in TE polarizations, which is formulated by the governing eigenequation (4) and the BC Eq. (6).

III. PML APPROACH

A. Damping functions

As illustrated in the left panel of Fig. 2, the method is implemented by introducing an absorption layer, called a per-
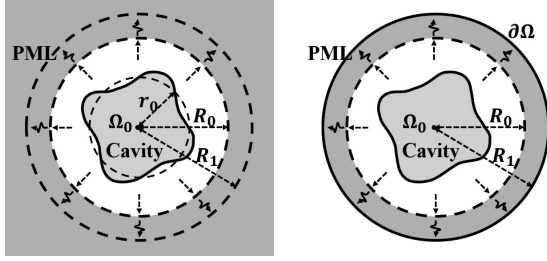
FIG. 2. Schematic illustration of the perfectly matched layer (PML). The left panel is an illustration of the PML, starting from the far-field region and extending to infinity. The right panel shows the truncated PML.

fectly matched layer (PML). In Fig. 2, r_0 roughly stands for the cavity radius and should be specified for each particular cavity shape. The PML starts at the radius of R_0, and we consider that the PML extends to infinity for method development in this subsection. For computational purposes in the following subsections, the PML will be truncated at the radius of R_1; see the right panel of Fig. 2.

The absorption is realized by constructing a dimensionless damping function $\tilde{\sigma}(r)$ as

$$\tilde{\sigma}(r) = \begin{cases} 0, & 0 \leqslant r < R_0, \\ \text{increasing}, & R_0 \leqslant r \leqslant R_1, \\ \sigma_0, & r > R_1, \end{cases} \tag{9}$$

with some real-valued constant $\sigma_0 > 0$. The damping function should be second-order differentiable in the positive semiaxis, i.e., $\tilde{\sigma}(r) \in C^2(\mathbb{R}^+)$. A typical $C^2(\mathbb{R}^+)$ function with the above properties satisfied in the interval $[R_0, R_1]$ is given [42] by

$$\tilde{\sigma}(r) = \sigma_0 \frac{\int_{R_0}^{r} (t - R_0)^2 (R_1 - t)^2 dt}{\int_{R_0}^{R_1} (t - R_0)^2 (R_1 - t)^2 dt}. \tag{10}$$

However, the exact form of $\tilde{\sigma}(r)$ is not limited to Eq. (10), and any $C^2(\mathbb{R}^+)$ functions satisfying Eq. (9) are acceptable.

B. Complex-coordinate stretching

The PML methods can be viewed as complex stretching in coordinate systems. With the damping function $\tilde{\sigma}(r)$, complex-valued variables (ρ, ϕ) can be constructed based on the real-valued coordinate system (r, θ) as

$$\rho(r, \theta) = r[1 + i\tilde{\sigma}(r)], \tag{11a}$$

$$\phi(r, \theta) = \theta. \tag{11b}$$

The relations of partial derivatives between the two coordinate systems are explicitly expressed as

$$\frac{\partial}{\partial \rho} = \frac{1}{1 + i\sigma(r)} \frac{\partial}{\partial r}, \tag{12a}$$

$$\frac{\partial}{\partial \phi} = \frac{\partial}{\partial \theta}, \tag{12b}$$

in which we introduce the notation

$$\sigma(r) := \frac{d(r\tilde{\sigma}(r))}{dr} = \tilde{\sigma}(r) + r\frac{d\tilde{\sigma}(r)}{dr}. \tag{13}$$

For notation-simplification purposes, we also introduce two dimensionless variables $\alpha(r)$ and $\beta(r)$ as

$$\alpha(r) = 1 + i\tilde{\sigma}(r), \tag{14}$$

$$\beta(r) = 1 + i\sigma(r), \tag{15}$$

which are also called coordinate stretching variables in Ref. [52].

C. Damping eigenequations

The original eigenequation (4) under a polar-coordinate system is

$$\frac{1}{r}\frac{\partial}{\partial r}\left(\frac{r}{\varepsilon(r, \theta)}\frac{\partial \psi(r, \theta)}{\partial r}\right) + \frac{1}{r^2}\frac{\partial}{\partial \theta}\left(\frac{1}{\varepsilon(r, \theta)}\frac{\partial \psi(r, \theta)}{\partial \theta}\right) + k^2\psi(r, \theta) = 0. \tag{16}$$

Replacing the real-valued coordinate system (r, θ) with the complex-valued variables (ρ, ϕ) leads to the damping eigenequation. With the relations between coordinate systems Eq. (11) and their derivatives Eq. (12), the damping eigenequation can be explicitly expressed under the real-valued system as

$$\frac{1}{r\alpha(r)\beta(r)}\frac{\partial}{\partial r}\left(\frac{r\alpha(r)}{\varepsilon(r, \theta)\beta(r)}\frac{\partial \psi(r, \theta)}{\partial r}\right)$$
$$+ \frac{1}{r^2\alpha^2(r)}\frac{\partial}{\partial \theta}\left(\frac{1}{\varepsilon(r, \theta)}\frac{\partial \psi(r, \theta)}{\partial \theta}\right)$$
$$+ k^2\psi(r, \theta) = 0. \tag{17}$$

We then change the coordinates from a polar system to a Cartesian system. To avoid confusion, we use the notation $\varepsilon(\boldsymbol{r})$ to denote the dielectric functions in $\mathbb{R}^2$ without specifying the coordinate system being used. The damping eigenequation under the Cartesian-coordinate system is expressed as

$$\frac{\partial}{\partial x}\left[\left(\frac{x^2}{\beta^2} + \frac{y^2}{\alpha^2}\right)\frac{1}{r^2\varepsilon}\frac{\partial \psi}{\partial x} + \left(\frac{1}{\beta^2} - \frac{1}{\alpha^2}\right)\frac{xy}{r^2\varepsilon}\frac{\partial \psi}{\partial y}\right]$$
$$+ \frac{\partial}{\partial y}\left[\left(\frac{1}{\beta^2} - \frac{1}{\alpha^2}\right)\frac{xy}{r^2\varepsilon}\frac{\partial \psi}{\partial x} + \left(\frac{x^2}{\alpha^2} + \frac{y^2}{\beta^2}\right)\frac{1}{r^2\varepsilon}\frac{\partial \psi}{\partial y}\right]$$
$$+ \frac{1}{\alpha\beta^3\varepsilon}\frac{d(\alpha\beta)}{dr}\left(\frac{x}{r}\frac{\partial \psi}{\partial x} + \frac{y}{r}\frac{\partial \psi}{\partial y}\right) + k^2\psi = 0. \tag{18}$$

To simplify the damping eigenequation, the matrix $A(\boldsymbol{r})$ is introduced [28] as

$$A(\boldsymbol{r}) := \frac{1}{r^2}\begin{pmatrix} \frac{x^2}{\beta^2} + \frac{y^2}{\alpha^2} & \frac{xy}{\beta^2} - \frac{xy}{\alpha^2} \\ \frac{xy}{\beta^2} - \frac{xy}{\alpha^2} & \frac{x^2}{\alpha^2} + \frac{y^2}{\beta^2} \end{pmatrix}, \tag{19}$$

and the damping eigenequation (18) can be simplified as

$$\boldsymbol{\nabla} \cdot \left(\frac{1}{\varepsilon(\boldsymbol{r})}A\boldsymbol{\nabla}\psi\right) + \frac{1}{\alpha\beta^3\varepsilon(\boldsymbol{r})}\boldsymbol{\nabla}(\alpha\beta) \cdot \boldsymbol{\nabla}\psi + k^2\psi = 0. \tag{20}$$

In the region $r < R_0$, the matrix $A(\boldsymbol{r})$ becomes the 2-by-2 identity matrix and $\boldsymbol{\nabla}(\alpha\beta) \equiv 0$, meaning that the damping eigenequation (20) reduces to the original eigenequation (4). This indicates that the eigenfunctions remain unchanged in the region $r < R_0$ as if the PML does not exist.

D. Exponentially decaying boundary conditions

Although the damping eigenequation (20) looks more complicated than the original eigen-equation (4), it avoids the original exponentially growing BC Eq. (6). Replacing the real-valued coordinate system (r, θ) with complex-valued variables (ρ, ϕ) in Eq. (6), the BC becomes, as $r \to +\infty$,

$$\psi(r, \theta) \sim \frac{F(\phi)}{\sqrt{\rho}} e^{in_0 k\rho} = \frac{F(\theta)}{\sqrt{(1 + i\sigma_0)r}} e^{in_0(k_r - ik_i)(1 + i\sigma_0)r}$$

$$= \frac{F(\theta)}{\sqrt{(1 + i\sigma_0)r}} e^{in_0(k_r + k_i\sigma_0)r} e^{-n_0(k_r\sigma_0 - k_i)r}. \tag{21}$$

As given in Eq. (21), the BC associated with the damping eigenequation (20) is exponentially decaying if the preset parameter σ_0 is large enough, i.e., $\sigma_0 > k_i/k_r = 1/(2Q)$.

E. Domain truncation

Since the BC for the damping eigenequation is exponentially decaying, it is appropriate to approximate the problem by truncating the original domain $\mathbb{R}^2$ into a finite region Ω, as shown in the right panel of Fig. 2. The underlying mechanism of the PML method is to introduce a sufficient amount of damping in the absorption region so that outgoing waves decay to almost zero at the outer edge of the PML, so that we can apply the Dirichlet BC at the outer edge of the PML, i.e.,

$$\psi|_{\partial\Omega} = 0. \tag{22}$$

The thickness of the PML can be obtained by estimating how close the field decays to zero at $\partial\Omega$. We introduce γ as the exponent of the exponential decay factor $e^{-\gamma} = e^{-n_0(k_r\sigma_0 - k_i)d}$ when the field propagates to $\partial\Omega$. By equaling the exponent, a typical PML thickness d (with $d = R_1 - R_0$) is given as

$$d = \frac{\gamma}{n_0(k_r\sigma_0 - k_i)} \approx \frac{\gamma}{n_0 k_r \sigma_0}. \tag{23}$$

Normally, we can set $\gamma = 10$ with $e^{-10} = 4.5 \times 10^{-5}$ or $\gamma = 20$ with $e^{-20} = 2 \times 10^{-9}$, meaning that the field decays to almost zero at $\partial\Omega$ so that the Dirichlet BC (22) is effective.

IV. FINITE-ELEMENT METHODS FOR THE DAMPING EIGENPROBLEM

As with the derivation shown above, solving the original resonance problem is equivalent to solving the damping eigenproblem, with governing Eq. (20) and Dirichlet BC Eq. (22). In this section we develop a finite-element method (FEM) to compute the numerical solutions to the damping eigenproblem.

We first derive the weak form for the damping eigenequation (20). Here, we use the notation $H_0^1(\Omega)$ to stand for the Hilbert space in which the function and its derivatives are square-integrable and vanishes on the boundary:

$$H_0^1(\Omega) := \left\{ f \in L^2(\Omega) : \int_\Omega (|f|^2 + |\nabla f|^2) d\mu < +\infty \quad \text{and} \quad f|_{\partial\Omega} = 0 \right\}. \tag{24}$$

The eigenfunctions are assumed to be in this Hilbert space, i.e., $\psi \in H_0^1(\Omega)$. The weak form for the damping eigenequation (20) can be derived, for $\forall \varphi \in H_0^1(\Omega)$, as

$$\int_\Omega \frac{1}{\varepsilon(\boldsymbol{r})} \nabla\varphi \cdot (A(\boldsymbol{r})\nabla\psi) d\mu - \int_\Omega \frac{\varphi}{\alpha\beta^3\varepsilon(\boldsymbol{r})} \nabla(\alpha\beta) \cdot \nabla\psi \, d\mu = k^2 \int_\Omega \varphi\psi \, d\mu. \tag{25}$$

In the weak form Eq. (25), the bilinear form on the left-hand side,

$$P(\varphi, \psi) := \int_\Omega \frac{1}{\varepsilon(\boldsymbol{r})} \nabla\varphi \cdot (A(\boldsymbol{r})\nabla\psi) d\mu - \int_\Omega \frac{\varphi}{\alpha\beta^3\varepsilon(\boldsymbol{r})} \nabla(\alpha\beta) \cdot \nabla\psi \, d\mu, \tag{26}$$

is the coupling strength between φ and ψ. The bilinear form on the right-hand side,

$$Q(\varphi, \psi) := \int_\Omega \varphi\psi \, d\mu, \tag{27}$$

is the coupling energy between φ and ψ.

The FEM formulation is implemented by approximating the infinite-dimensional space $H_0^1(\Omega)$ with a finite-element space. We first generate a triangular mesh M_h on the domain Ω. In each triangle, there are six points (x_i, y_i), including three vertices and three midpoints. Based on the six points, we build six element-functions ξ_i in Lagrangian P2 form, i.e., for $\forall(x, y) \in M_h$,

$$\xi_i(x, y) = A + Bx + Cy + Dx^2 + Exy + Fy^2, \tag{28}$$

$$\text{satisfying} \quad \xi_i(x_j, y_j) = \delta_{ij}, \tag{29}$$

where δ_{ij} is the Kronecker notation. Assembling element functions of different triangles but associated with the same point forms the basis functions φ_j. All the basis functions φ_j form the finite-element space V_h. The eigensolution of Eq. (25) is approximated as linear combinations of the basis functions in V_h:

$$\psi = \sum_{\varphi_j \in V_h} c_j \varphi_j. \tag{30}$$

In the weak form Eq. (25), substituting the above representation of ψ and varying φ as all basis functions $\varphi_j \in V_h$ generate the matrix representation of the damping eigenequation:

$$\widetilde{P}\Psi = k^2 \widetilde{Q}\Psi, \tag{31}$$

where the eigenvalue is k^2 and the eigenvector is $\Psi = (\dots, c_{j-1}, c_j, c_{j+1}, \dots)^T$. The $\widetilde{P}$ and $\widetilde{Q}$ are square matrices

with entities specified as

$$\widetilde{P}_{ij} = P(\varphi_i, \varphi_j), \tag{32}$$

$$\widetilde{Q}_{ij} = Q(\varphi_i, \varphi_j). \tag{33}$$

The algebraic eigenequation (31) is solved by the implicitly restarted Arnoldi method using ARPACK [53]. All the numerical processes, including generating meshes, building finite elements, matrix assembling, and matrix computations, are done using the open-source software FREEFEM++ [54].

V. COMPUTATIONAL RESULTS

In this section, we present three computational examples for different cavity shapes. We first study the eigenstates in the circular cavity, and we validate the PML method by comparing numerical results with existing analytical results. We then study the mode symmetries in the elliptic cavity. Finally, we trace the evolution of a pair of degenerate eigenstates when the cavity shape deforms smoothly from circle to square.

In all three computational examples, we set $R_0 = 3r_0$, and the PML region is truncated at $R_1 = 4r_0$. That is, the computational domain is defined as $\Omega := \{(x, y) : x^2 + y^2 \leqslant R_1^2\}$. The damping function is set as

$$\tilde{\sigma}(r) = \begin{cases} 0, & r \leqslant R_0, \\ \sigma_0 (r - R_0)^4, & R_0 < r \leqslant R_1, \end{cases} \tag{34}$$

where the region $r > R_0$ is truncated and σ_0 is set to be 1. We set the damping function as the polynomial of fourth order for the purpose of introducing enough damping into the PML. Other orders or other forms for the damping function would also work for the calculation as long as they introduce enough damping in the PML. We also set the dielectric permittivity as a piecewise-constant function, i.e.,

$$\varepsilon(\boldsymbol{r}) = \begin{cases} n_1^2, & \boldsymbol{r} \in \Omega_0, \\ n_0^2, & \boldsymbol{r} \in \Omega / \Omega_0, \end{cases} \tag{35}$$

where Ω_0 stands for the cavity domain. The refractive indices are n_1 and n_0 for the inside and outside of the cavity, respectively. For the three computational examples in this paper, we set $n_1 = 2$ and $n_0 = 1$.

A. Whispering-gallery modes in the circular cavity

Exact analytical solutions exist for the eigenstates in the circular cavity $\Omega_0 = \{(x, y) : x^2 + y^2 \leqslant r_0^2\}$. Those eigenstates are formed due to total internal reflections, and they are called whispering-gallery modes (WGMs) [22,23]. The eigenfunctions for WGMs in circular cavities are given [11,23] as

$$\psi(r, \theta) = \begin{cases} \dfrac{J_m(n_1 k r)}{J_m(n_1 k r_0)} e^{\pm i m \theta} & \text{for } r \leqslant r_0, \\[3mm] \dfrac{H_m(n_0 k r)}{H_m(n_0 k r_0)} e^{\pm i m \theta} & \text{for } r > r_0, \end{cases} \tag{36}$$

where J_m is the Bessel function of mth order, and H_m is the first-type Hankel function of mth order.

Maxwell's equations require that ψ and $\frac{1}{\varepsilon} \frac{\partial \psi}{\partial r}$ are continuous across the interface between the cavity inside and outside,
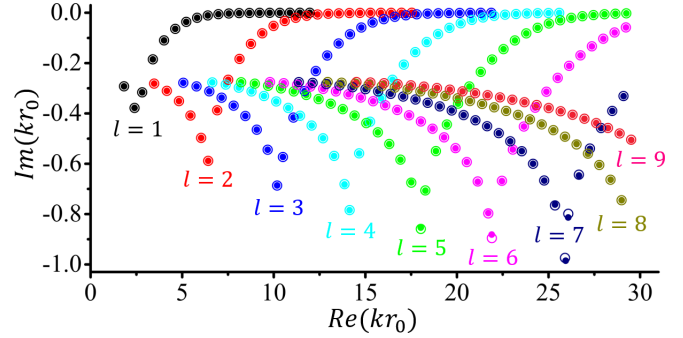

FIG. 3. Dimensionless eigenvalues of eigenstates for the circular cavity for the first nine radial orders $l = 1, 2, 3, 4, \ldots, 9$. The circles are eigenvalues computed using the developed PML method; the dots are eigenvalues obtained by finding numerical roots of the transcendental Eq. (37).

which leads to the eigencondition [11]

$$\frac{1}{n_1} \frac{J_m'(n_1 k r_0)}{J_m(n_1 k r_0)} = \frac{1}{n_0} \frac{H_m'(n_0 k r_0)}{H_m(n_0 k r_0)} \tag{37}$$

for any positive integer m. The eigencondition Eq. (37) gives a family of transcendental equations in terms of k. For each integer m, numerical roots of the transcendental equation can be found and rearranged in absolute-value ascending order, indexed by l. As a result, each eigenvalue $k_{m,l}$ in the circular cavity can be labeled by the mode number (m, l), where m is the azimuthal order and l is the radial order. With the eigenvalue $k_{m,l}$, the associated eigenfunction $\psi_{m,l}$ can be obtained by substituting the eigenvalue back into Eq. (36).

Using the PML method, we calculate the eigenvalues of WGMs for the first nine radial orders $l = 1, 2, 3, 4, \ldots, 9$, as shown in Fig. 3. The eigenvalues obtained by computing the roots of Eq. (37) are also plotted in Fig. 3 for comparison purposes. For each fixed radial order l, the plot of eigenvalues $k r_0$ forms a V-shape scatter-plot with an infinitely long right tail. The imaginary part of $k r_0$ is negative and approaches zero when $m \to \infty$. The computed eigenvalues are compared with the numerical roots of Eq. (37). As shown in Fig. 3, the results from the PML method and the roots of the eigencondition are in perfect agreement. Only a very minor deviation is observed when the imaginary part of the eigenvalue grows, where the minor deviation could be further reduced by introducing more damping in the PML, i.e., tuning σ_0 larger.

We also compute the eigenfunctions of WGMs and compare them with the analytical results. Figure 4 shows the modulus square of computed eigenfunctions. All the computed eigenfunctions are associated with azimuthal order $m = 7$, i.e., there are seven periods in the azimuthal direction. Each period contains one positive and one negative maximum in eigenfunctions, thus there are in total $2m = 14$ local maxima along the azimuthal direction in all plots of Fig. 4. The radial order l indicates the number of local maxima in the radial direction. In Fig. 4, the top four plots are the results computed by the PML method and the bottom four plots are the results calculated by the analytical formula Eq. (36). Because of the rotational symmetry of the circular cavity, there is a twofold degeneracy for each mode index (m, l), i.e., clockwise (CW) and counterclockwise (CCW), and any combination of CW
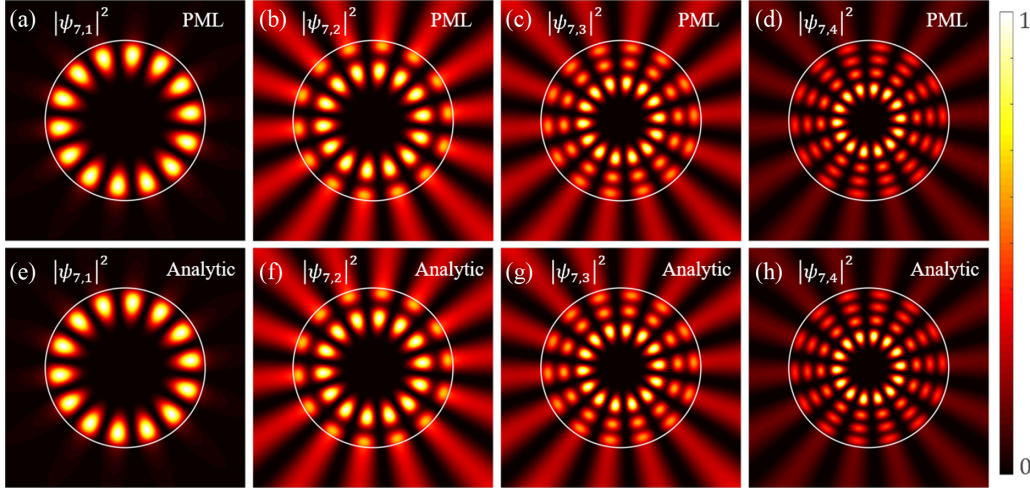
FIG. 4. Modulus square of the eigenfunctions for the circular cavity. Parts (a), (b), (c), and (d) are calculated by the PML method. Parts (e), (f), (g), and (h) are calculated by the analytical formula Eq. (36). The four columns are associated with the first four radial orders. All plots are associated with the azimuthal order $m = 7$.

and CCW is also an eigenfunction associated with the same eigenvalue, as indicated by the analytical solutions Eq. (36). The CW-CCW degeneracy is so sensitive to perturbations that tiny rounding errors in the computation would split the degeneracy. We note here that small perturbations are in general inevitable in numerical methods. The plots in the top row of Fig. 4 are the PML results with rounding errors, i.e., the degeneracy is split due to rounding errors. The plots in the bottom row of Fig. 4 are analytical results with a tuned combination of CW and CCW in order to compare with the PML results. We only plot and compare one pair for each mode index in Fig. 4, and the comparison results of another pair are similar. Those plots of the mode distribution show that the eigenfunctions calculated by the PML method are also perfectly matched with the analytic results.
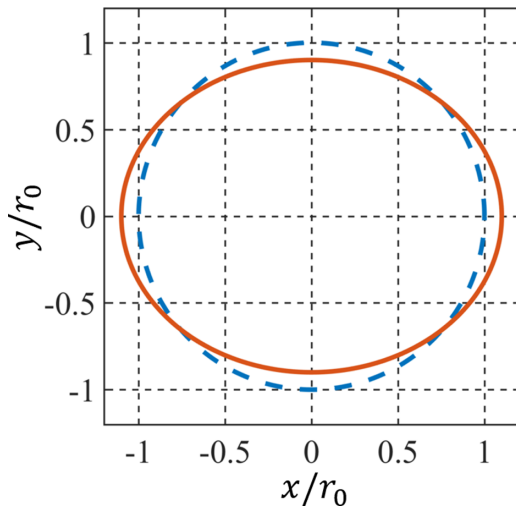
As shown in Figs. 3 and 4, the computed eigenvalues and mode distributions using the PML method both agree perfectly with the existing analytical results. This demonstrates that the PML method developed in this paper is efficient and accurate in computing optical eigenstates. Note that the comparison conducted in this subsection is for validation purposes. It is more interesting to find optical modes associated with deformed cavities, for which analytical solutions are in general not available. In the next two computational examples, we will apply the PML method to deformed cavities.

B. Optical eigenstates in the elliptic cavity

In this subsection, we apply the PML method to study chaotic eigenstates in elliptic cavities, whose shapes in the Cartesian-coordinate system are given by

$$\frac{x^2}{(r_0 + \delta)^2} + \frac{y^2}{(r_0 - \delta)^2} = 1, \tag{38}$$

FIG. 5. The solid line shows the elliptic shape with semimajor axis $a = r_0 + \delta$ and semiminor axis $b = r_0 - \delta$, where the parameter $\delta = 0.1 r_0$. The dashed line shows the circular shape with radius $r_0 = 1$.
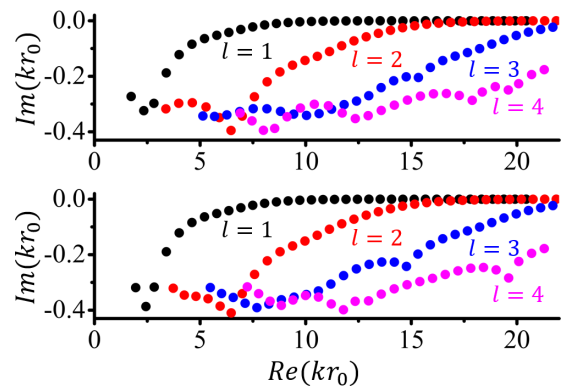

FIG. 6. Dimensionless eigenvalues of eigenstates of the elliptic cavity for the first four radial orders $l = 1$, 2, 3, and 4. The top panel shows the eigenvalues of *even* modes, and the bottom panel shows the eigenvalues of *odd* modes.
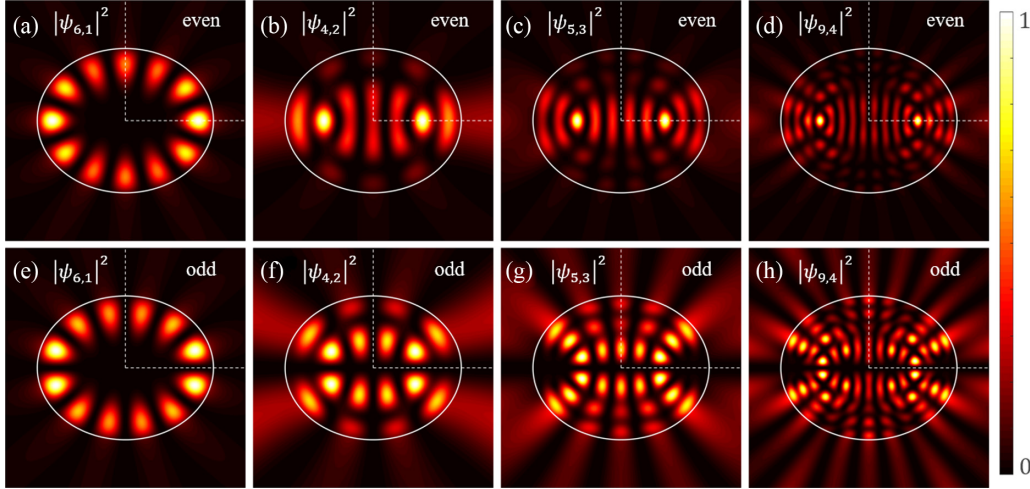
FIG. 7. Modulus square of eigenfunctions of the elliptic cavity. The top row shows the *even* modes, and the bottom row shows the *odd* modes. (a),(e) $(m, l) = (6, 1)$; (b),(f) $(m, l) = (4, 2)$; (c),(g) $(m, l) = (5, 3)$; (d),(h) $(m, l) = (9, 4)$. The dashed lines are the positive x-axis and the positive y-axis. The *even* and *odd* symmetries are with respect to the x-axis.

or in the polar-coordinate system by

$$R(\theta) = \frac{r_0^2 - \delta^2}{\sqrt{(r_0 - \delta)^2 \cos^2(\theta) + (r_0 + \delta)^2 \sin^2(\theta)}}. \quad (39)$$

In this computational example, we choose parameters $r_0 = 1$ and $\delta = 0.1r_0$. This elliptic cavity compared with the circular cavity is shown in Fig. 5.

The CW-CCW degeneracy is formed due to rotational symmetry of the disk cavity. For the elliptic cavity, the rotational symmetry is broken and the degenerate eigenstates split. However, the elliptic cavity still has axial symmetry with respect to the x-axis and the y-axis. As a result, the eigenfunctions of the optical eigenstates are also symmetric with respect to the x-axis and the y-axis, and the eigenstates are characterized as *even* modes and *odd* modes.

We first compute the eigenvalues of the optical eigenstates in the elliptic cavity for the first four radial orders $l = 1, 2, 3,$ and 4. The eigenvalues for the *even* and *odd* modes are shown in Fig. 6. As in the case of the circular cavity, the eigenvalues of each radial order l exhibit an infinitely long right tail. The imaginary part of kr_0 is negative and approaches zero when the real part kr_0 approaches infinity. Unlike the degenerate states in the circular cavity, the eigenvalues for *even* and *odd* modes in the elliptic cavity are split, thus they are distinguishable. The overall trends of the eigenvalues are similar to those degenerate cases in the circular cavity shown in Fig. 3.

Figure 7 shows mode distributions of those four pairs of eigenstates in the elliptic cavity. In this paper, the *even* modes and the *odd* modes of eigenfunctions in the elliptic cavity are with respect to the x-axis. As shown in the top row of Fig. 7, the eigenfunctions of the *even* modes are axial-symmetric with respect to the x-axis, i.e.,

$$\psi(r, -\theta) = \psi(r, \theta). \quad (40)$$

In contrast, as shown in the bottom row of Fig. 7, the eigenfunctions of the *odd* modes are central symmetric with respect to the x-axis, i.e.,

$$\psi(r, -\theta) = -\psi(r, \theta), \quad (41)$$

so that the eigenfunctions vanish along the x-axis for all *odd* modes, i.e., $\psi(r, 0) = \psi(r, \pi) \equiv 0$ for all $r \in \mathbb{R}^+$. The above *even* and *odd* symmetries are referred with respect to the x-axis. However, the elliptic cavity is also axial-symmetric with respect to the y-axis. Similar symmetry behaviors of the eigenfunctions also hold with respect to the y-axis. In general, the symmetry behavior holds for any axial symmetric cavity with respect to its corresponding symmetric axis. As shown in Fig. 7, when the mode index (the azimuthal order or radial order) of the eigenstates increases, the mode distributions become more and more irregular.

C. Evolution of eigenstates in cavity deformations

Although the optical eigenstates in both circular cavities and square cavities are widely applied in on-chip devices, the relations between the eigenstates in the two generic shapes
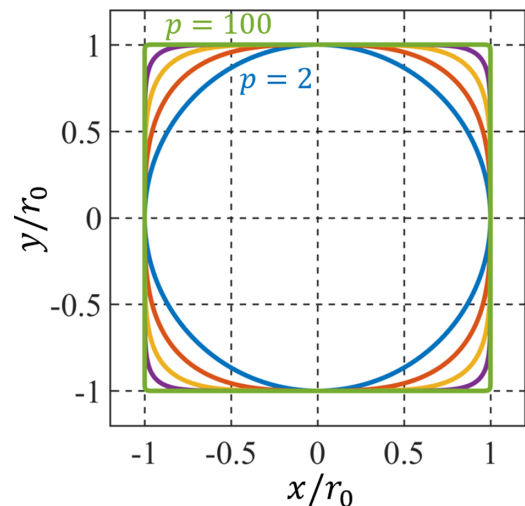

FIG. 8. Several vector-norm shapes defined as Eq. (42) for p varies from 2 to 100. The blue line, $p = 2$, is the circular shape. The green line, $p = 100$, is the square shape.
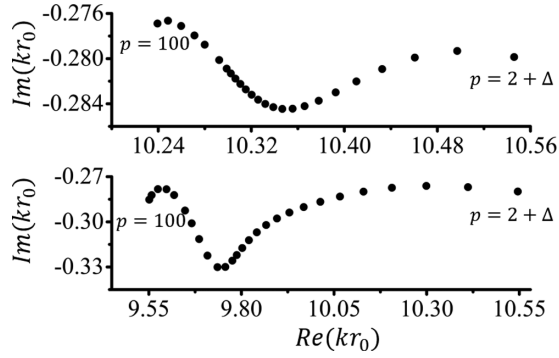
FIG. 9. Dimensionless eigenvalues of eigenstates in the vector-norm-shaped cavities. The top panel is eigenvalues for the *even* modes, and the bottom panel is eigenvalues for the *odd* modes. Parameter $\Delta = 10^{-4}$.

have not been clearly studied. We are interested in how the eigenstates in the circular cavity evolve to those in the square cavity. In this subsection, we trace a pair of degenerate eigenstates when the cavity-shape deforms from a circle to a square.

To trace the evolution of the eigenstates, we first set up cavity shapes that smoothly deform from a circle to a square [55], which is defined as the unit p-norm in the Cartesian-coordinate system as

$$|x|^p + |y|^p = r_0^p, \tag{42}$$

or in the polar-coordinate system as

$$R(\theta) = r_0(|\cos(\theta)|^p + |\sin(\theta)|^p)^{-1/p}. \tag{43}$$

We call this cavity shape the vector-norm shape. When $p = 2$, the vector-norm shape is a circle; when $p = +\infty$, the vector-norm shape is a square. The vector-norm shape smoothly deforms from a circle to a square as p gradually changes from 2 to $+\infty$. Figure 8 illustrates the vector-norm shapes for several p values between 2 and 100. In the following, we use the vector-norm shape of $p = 2$ to represent the circle, and

we use the vector-norm shape of $p = 100$ to approximate the square.

In the eigenstates evolution, we focus on a pair of WGMs, i.e., $(m, l) = (2, 6)$. This pair of WGMs are degenerate eigenstates in the circular cavity, but they will evolve into different eigenstates when the cavity shape deforms to a square. We first trace the eigenvalues when p varies. Figure 9 shows the eigenvalue evolution of the degenerate pair. As p varies from 2 to 100, the real part of the eigenvalue decreases while the imaginary part oscillates. As shown in Fig. 9, the eigenvalues of the mode pair are largely deviated when $p = 100$ (see the real part), which indicates that the degenerate WGM pair evolves into different states when the cavity shape deforms to a square.

As in the elliptic cavity, the vector-norm shape is also axial symmetric. For any value p, the vector-norm shape is axial-symmetric with respect to both the x-axis and the y-axis as well as the line $x + y = 0$ and the line $x - y = 0$. Therefore, the previous axis symmetry behaviors of eigenfunctions, e.g., Eqs. (40) and (41), also hold here for the mode pairs throughout their evolution, with respect to the corresponding axial-symmetric axis.

Figure 10 shows the evolution of mode distributions in the vector-norm cavity as the shape deforms from a circle to a square. The eigenstate pair with index $(m, l) = (2, 6)$ are degenerate in the circular cavity ($p = 2$), thus they are not able to be distinguished. However, once the shape is slightly deformed, i.e., $p = 2 + \Delta$ for any small $\Delta > 0$, the pair of degenerate eigenstates would split into one *even* mode and one *odd* mode; see Figs. 10(a) and 10(f). Again, the *even* and *odd* symmetry in this subsection are with respect to the x-axis. As the cavity shape deforms, the eigenfunctions of the mode pair evolve in different directions, but the symmetry of eigenstates is preserved in the mode evolution as shown in Fig. 10. When $p = 100$, the cavity shape becomes a square, and the mode distributions are the eigenstates of the square cavity.

As shown in the eigenvalue plot (Fig. 9) and the evolution of eigenfunctions (Fig. 10), the degenerate eigenstate
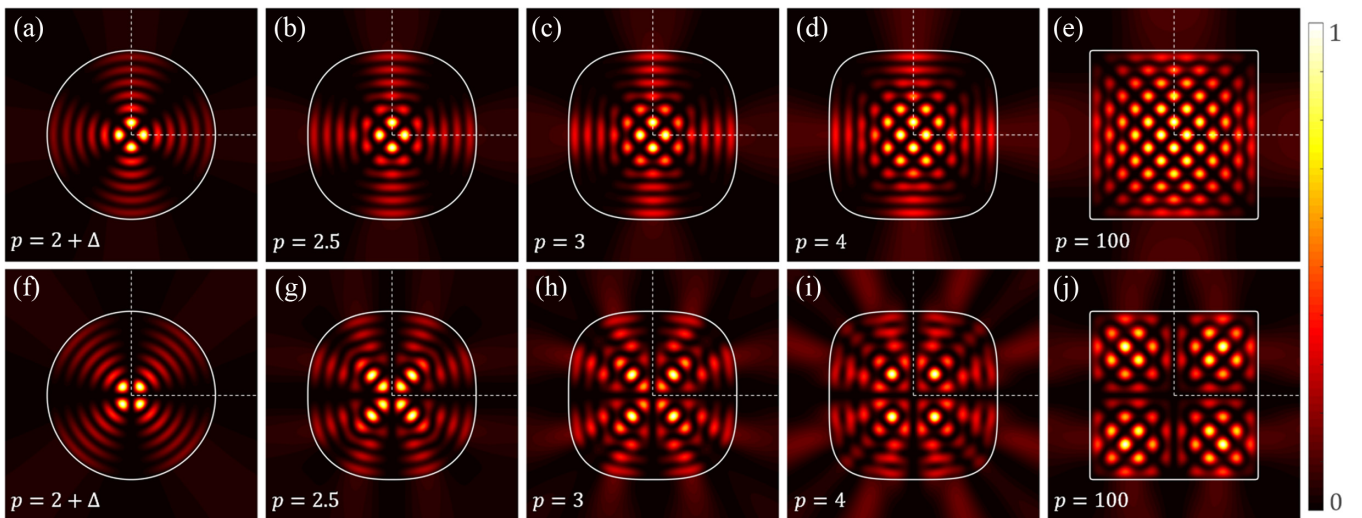

FIG. 10. Modulus square of eigenfunctions as the cavity shape deforms from circle to square. The top row shows the *even* modes, and the bottom row shows the *odd* modes. (a),(f) $p = 2 + \Delta$ with $\Delta = 10^{-4}$; (b),(g) $p = 2.5$; (c),(h) $p = 3$; (d),(i) $p = 4$; (e),(j) $p = 100$. The dashed lines are the positive x-axis and the positive y-axis. Here, the *even* and *odd* symmetries are with respect to the x-axis.

pair evolves into completely different eigenstates after cavity deformations. This tracing method can be applied for other eigenstate pairs throughout cavity deformations. It can be observed from Figs. 9 and 10 that the degenerate eigenstate pairs evolve in different directions when the cavity shape deforms, whereas the mode symmetry is preserved during the evolution.

VI. CONCLUSIONS

Based on the complex-stretching technique, we have developed a numerical method to compute the transverse-electric polarized optical eigenstates in the 2D dielectric systems. The method is implemented by constructing in the far-field region an absorption layer. The optical eigenstates in the dielectric cavity are leaky modes with energy radiating to infinity, resulting in the exponentially growing BC. The complex stretching technique transforms the BC from exponential growing into exponential decaying, and it leads to the damping eigenequation. With a sufficient amount of damping introduced in the PML, the infinite domain can be truncated into a finite region. We have derived the weak form of the damping eigenequation in the truncated domain to implement finite-element methods for computing the eigenstates.

The developed PML method is first applied to the circular cavity, and the obtained results agree perfectly with existing analytical results. We then apply the PML method to the elliptic cavity to study the chaotic optical eigenstates, where degenerate pairs are found splitting into *even-* and *odd*-symmetric modes. Finally, we apply the PML method to study the eigenstate evolution in the vector-norm shape cavities. We set up the cavity shape to gradually deform from a circle to a square, and we trace a degenerate pair throughout the deformation. The degenerate pair evolves into different states when the cavity deforms into a square, but the *even* and *odd* axial symmetry is preserved throughout the deformation. The PML method developed in this paper does not impose any requirement on the dielectric distributions, therefore it is applicable to arbitrary dielectric systems, including largely deformed cavities, multicavities, random media, index-varying materials, etc.

[1] A. Novack, M. Streshinsky, R. Ding, Y. Liu, A. E.-J. Lim, G.-Q. Lo, T. Baehr-Jones, and M. Hochberg, Nanophotonics **3**, 205 (2014).

[2] K. J. Vahala, Nature (London) **424**, 839 (2003).

[3] K. Djordjev, S.-J. Choi, S.-J. Choi, and R. D. Dapkus, IEEE Photon. Technol. Lett. **14**, 828 (2002).

[4] V. R. Almeida, C. A. Barrios, R. R. Panepucci, and M. Lipson, Nature (London) **431**, 1081 (2004).

[5] Y. Zhang, Y. Li, S. Feng, and A. W. Poon, IEEE J. Sel. Top. Quantum Electron. **20**, 136 (2014).

[6] S. L. McCall, A. F. J. Levi, R. E. Slusher, S. J. Pearton, and R. A. Logan, Appl. Phys. Lett. **60**, 289 (1992).

[7] D. Liang and J. E. Bowers, Nat. Photon. **4**, 511 (2010).

[8] L. He, Ş. K. Özdemir, J. Zhu, W. Kim, and L. Yang, Nat. Nanotechnol. **6**, 428 (2011).

[9] F. Vollmer and L. Yang, Nanophotonics **1**, 267 (2012).

[10] S. Sunada and T. Harayama, Opt. Express **15**, 16245 (2007).

[11] R. Dubertrand, E. Bogomolny, N. Djellali, M. Lebental, and C. Schmit, Phys. Rev. A **77**, 013804 (2008).

[12] T. Jiang and Y. Xiang, Phys. Rev. A **99**, 023847 (2019).

[13] J.-W. Ryu, S. Rim, Y.-J. Park, C.-M. Kim, and S.-Y. Lee, Phys. Lett. A **372**, 3531 (2008).

[14] C. P. Dettmann, G. V. Morozov, M. Sieber, and H. Waalkens, Europhys. Lett. **87**, 34003 (2009).

[15] C. M. Bender, Rep. Prog. Phys. **70**, 947 (2007).

[16] H. Cao and J. Wiersig, Rev. Mod. Phys. **87**, 61 (2015).

[17] E. S. C. Ching, P. T. Leung, A. Maassen van den Brink, W. M. Suen, S. S. Tong, and K. Young, Rev. Mod. Phys. **70**, 1545 (1998).

[18] J. U. Nöckel and A. D. Stone, Nature (London) **385**, 45 (1997).

[19] N. B. Rex, H. E. Tureci, H. G. L. Schwefel, R. K. Chang, and A. D. Stone, Phys. Rev. Lett. **88**, 094102 (2002).

[20] M. Brandstetter, M. Liertzer, C. Deutsch, P. Klang, J. Schöberl, H. E. Türeci, G. Strasser, K. Unterrainer, and S. Rotter, Nat. Commun. **5**, 4034 (2014).

[21] W. D. Heiss, J. Phys. A **45**, 444016 (2012).

[22] L. Rayleigh, Philos. Mag. **20**, 1001 (1910).

[23] A. N. Oraevsky, Quantum Electron. **32**, 377 (2002).

[24] A. W. Poon, F. Courvoisier, and R. K. Chang, Opt. Lett. **26**, 632 (2001).

[25] Y.-D. Yang and Y.-Z. Huang, J. Phys. D **49**, 253001 (2016).

[26] J. Kullig and J. Wiersig, Phys. Rev. A **94**, 043850 (2016).

[27] J. Wiersig, J. Opt. A **5**, 53 (2002).

[28] T. Jiang and Y. Xiang, Phys. Rev. A **102**, 053704 (2020).

[29] J. U. Nöckel and A. D. Stone, in *Optical Processes in Microcavities* (World Scientific, Singapore, 1996) pp. 389–426.

[30] N. Moiseyev, *Non-Hermitian Quantum Mechanics* (Cambridge University Press, Cambridge, 2011).

[31] J.-P. Bérenger, J. Comput. Phys. **114**, 185 (1994).

[32] J.-P. Bérenger, J. Comput. Phys. **127**, 363 (1996).

[33] W. C. Chew and W. H. Weedon, Microwave Opt. Tech. Lett. **7**, 599 (1994).

[34] F. Teixeira and W. Chew, IEEE Microwave Guided Wave Lett. **7**, 371 (1997).

[35] F. Teixeira and W. Chew, in *IEEE Antennas and Propagation Society International Symposium 1997, Digest* (IEEE, Piscataway, NJ, 1997), Vol. 3, pp. 1908–1911.

[36] F. Collino and P. Monk, SIAM J. Sci. Comput. **19**, 2061 (1998).

[37] F. Collino and P. Monk, Comput. Methods Appl. Mech. Engrg. **164**, 157 (1998).

[38] M. Lassas and E. Somersalo, Computing **60**, 229 (1998).

[39] M. Lassas and E. Somersalo, Proc. R. Soc. Edinburgh: Sect. A Math. **131**, 1183 (2001).

[40] S. Hein, T. Hohage, and W. Koch, J. Fluid Mech. **506**, 255 (2004).

[41] F. Q. Hu, Int. J. Comput. Fluid Dyn. **18**, 513 (2004).

[42] S. Kim and J. E. Pasciak, Math. Comp. **78**, 1375 (2009).

[43] F. Teixeira and W. Chew, IEEE Microwave Guided Wave Lett. **8**, 223 (1998).

[44] F. Teixeira and W. Chew, J. Electromagn. Waves. Appl. **13**, 665 (1999).

[45] B. Donderici and F. L. Teixeira, IEEE Trans. Microwave Theor. Tech. **56**, 113 (2008).

[46] W. P. Huang, C. L. Xu, W. Lui, and K. Yokoyama, IEEE Photon. Tech. Lett. **8**, 652 (1996).

[47] J. P. Hugonin and P. Lalanne, J. Opt. Soc. Am. A **22**, 1844 (2005).

[48] C. Sauvan, J. P. Hugonin, I. S. Maksymov, and P. Lalanne, Phys. Rev. Lett. **110**, 237401 (2013).

[49] Z. Chen and H. Wu, SIAM J. Numer. Anal. **41**, 799 (2003).

[50] W. C. Chew, arXiv:2107.09672.

[51] J. D. Jackson, *Classical Electrodynamics*, 3rd ed. (Wiley, New York, 1999).

[52] W. Chew, J. Jin, and E. Michielssen, in *IEEE Antennas and Propagation Society International Symposium 1997, Digest* (IEEE, Piscataway, NJ, 1997), Vol. 3, pp. 2060–2063.

[53] R. B. Lehoucq, D. C. Sorensen, and C. Yang, *ARPACK Users' Guide: Solution of Large-Scale Eigenvalue Problems with Implicitly Restarted Arnoldi Methods* (SIAM, Philadelphia, 1998).

[54] F. Hecht, J. Numer. Math. **20**, 251 (2012).

[55] S. V. Boriskina, T. M. Benson, P. Sewell, and A. I. Nosich, IEEE J. Quantum Electron. **41**, 857 (2005).